frontiers | Frontiers in Earth Science

TYPE Original Research
PUBLISHED 23 January 2025
DOI 10.3389/feart.2025.1537337

OPEN ACCESS

EDITED BY
Weiyao Guo,
Shandong University of Science and Technology, China

REVIEWED BY
Peng Li,
University of Science and Technology Beijing, China
Huarui Hu,
Shenzhen University, China

*CORRESPONDENCE
Ruide Lei,
leiruide123@163.com

RECEIVED 30 November 2024
ACCEPTED 08 January 2025
PUBLISHED 23 January 2025

CITATION
Liu J and Lei R (2025) Role of hole depth on mechanical behavior and acoustic emission characteristics of pre-drilled sandstone. *Front. Earth Sci.* 13:1537337. doi: 10.3389/feart.2025.1537337

Role of hole depth on mechanical behavior and acoustic emission characteristics of pre-drilled sandstone

Jiahan Liu[1] and Ruide Lei[1,2]*

[1]College of Civil Engineering, Chongqing Jiaotong University, Chongqing, China, [2]College of Civil Engineering, Sichuan University of Science and Engineering, Zigong, China

To examine the influence of hole depth on the mechanical properties of rock, a series of uniaxial compression tests were performed on six groups of pre-drilled sandstone samples, each with varying depths. Also, multiple physical fields coupled with acoustic emission (AE) and digital image correlation (DIC) systems were synchronously employed to monitor the fracturing process. The study focused on characterizing the cracking fracturing, energy evolution, and fracture patterns in pre-drilled sandstones with different depths. The findings show that the peak strength of the sandstone decreases linearly with the increase of hole depth. The fracture mode transits from simple unilateral spalling to a complex fracture mode characterized by multiple fractures and spalling. AE analysis shows that the deeper the borehole, the lower the AE signal frequency, indicating fewer but more significant fracturing events. With the increase of hole depth, the peak elastic energy of the sample decreases from 29.81 kJ/m^3 to 22.65 kJ/m^3, and the dissipated energy increases from 4.48 kJ/m^3 to 6.25 kJ/m^3. Moreover, the AE energy of the pre-drilled sandstone displays distinct multifractal spectrum features under different stress levels. The multifractal spectrum width ($\Delta\alpha$) varies from 0.419 to 0.227, suggesting that small-scale fracturing events predominantly govern the failure mechanism. DIC observation shows that the major principal strain concentration mainly occurs around the hole. The monitoring points around the hole show that the cumulative strain at P2 and P6 is significantly higher compared to other regions. Furthermore, it is observed that the stress release pathways originating from newly formed cracks and dislocation slips become more diversified, suggesting a more complex fracturing mechanism.

KEYWORDS

crack classification, pre-drilled sandstone, acoustic emission, digital image correlation, multifractal

1 Introduction

In the process of sandstone diagenesis, the internal structure and mineral composition of sandstone in different regions are different. Sandstone, a typical heterogeneous material, contains numerous inherent defects such as joints, fractures, and voids (Wray, 2009; Yang et al., 2017; Sharafisafa et al., 2019; Wu et al., 2019). The presence of defects in rock results in an uneven distribution of the stress field, rendering it susceptible to failure along discontinuities during construction activities (Hu et al., 2022; Zou et al., 2023;

Huang et al., 2024; Zhang et al., 2024; Zhao et al., 2024). This poses significant challenges to the geothermal energy extraction, oil and gas production, and tunneling and mining operations. Natural rocks are normally filled with geo-materials that are of different elastic modulus from the host rock, such as rock debris and clay, forming close discontinuities, as shown in Figure 1. In rock engineering applications, the damage and failure usually initiate from or are caused by the weakness of embedded discontinuities (Feng et al., 2020; Qin et al., 2022; Gao et al., 2024). Therefore, gaining a comprehensive understanding of the localized deformation behavior and cracking process in void-filled rocks is essential for the secure construction of underground chambers and tunnel excavations.

Many scholars have conducted extensive laboratory testing and theoretical modeling to investigate the mechanical properties of rocks with prefabricated cracks or pores. Zhu et al. (2022) performed uniaxial compression tests to elucidate deformation and failure mechanism from the perspective of energy evolution. The findings suggest that inclusions enhance the strength and deformation capacity of rock samples, and they contribute to crack arrest during the initiation and propagation of new cracks. Li K. S. et al. (2024) employed a hybrid of experimental and numerical approaches to examine the compressive strength and crack mechanisms in porous marble. The results indicate that as the double-pore inclination angle increases, the crack initiation path shifts from the elliptical pore surface to a more direct transfer, and the failure mode varies from tension to shear, followed by a shift to tension-dominated, with the simulation outcomes closely aligning with experimental data. Du et al. (2023) investigated the impact of various filling states on the strength, deformation, fracture behavior, and permeability in sandstone using triaxial tests and X-ray CT technology. The results revealed that the infilling can enhance the rock's strength and deformation capabilities. The crack initiation point and propagation path can be changed. Zhou et al. (2021) conducted uniaxial compression tests on red sandstone samples containing both unfilled and filled dental defects. The results demonstrate that the infilling material can markedly influence the initiation and propagation of cracks. Despite extensive research on rock containing infillings, the investigation into the effect of hole depths on the mechanical behavior of rock masses, particularly their influence on crack propagation and fracture modes, remains insufficient.

In recent years, acoustic emission (AE) technology has emerged as a crucial tool for studying the micro-crack information that precedes macroscopic fracturing (Du et al., 2020; Du et al., 2022; Dong et al., 2023; Zheng et al., 2024). Zhang et al. (2017) investigated the AE characteristics of cracked rock materials under compression. The results show that the number of tensile and shear cracks increases with the loading rate. In addition, the frequency-amplitude relationship of AE signals follows a power-law distribution. Additionally, the frequency of AE events associated with cracks shows an exponential decay relationship. Liu Z. L. et al. (2022) have extended the research beyond circular hole fractures by investigating the triaxial extensional mechanical state of underground surrounding rock. Using a compression-tension load device, they studied the mechanical properties and failure modes of sandstone with various angles ranging from 0° to 60°. Their findings suggest that the failure mechanism transits from tensile crack to compressive crack, and the micro-fracture mode shifts from intergranular to transgranular as the inclination angle increases. Furthermore, Liu Z. L. et al. (2021) conducted uniaxial compression tests on cylindrical sandstone samples with the same crack length but different crack inclinations. They analyzed the mechanical properties, AE signals, and numerical simulation results of the specimens, demonstrating that the compressive strength of the specimens increases with the inclination angle. The elastic modulus also increases gradually with the crack inclination angle. Despite the advancements in AE technology, there are limitations to monitoring solely through AE signals. For example, it may struggle to capture the full spectrum of deformation characteristics (Chen et al., 2022; Dong et al., 2024; Liu J. et al., 2022). This is where the digital image correlation (DIC) method comes into play. As an optical measurement technology, DIC can effectively obtain real-time information about the full-field distribution of the material, allowing for the capture of crack deformation and propagation characteristics. The combination of AE and DIC technologies provides a more comprehensive understanding of the fracturing information related to crack initiation, propagation, and coalescence (Hebert and Khonsari, 2023; Yang et al., 2024; Wang et al., 2024a). This integrated approach enables multi-scale crack monitoring and analysis, ranging from the micro-to the macro-scale.

Based on the aforementioned reasons, uniaxial compression tests were conducted on pre-drilled sandstone containing prefabricated holes under varying depths, accompanied by simultaneous AE-DIC monitoring. Initially, the characteristics of AE signals of pre-drilled sandstone during the loading process were analyzed. The energy distribution and transformation during the

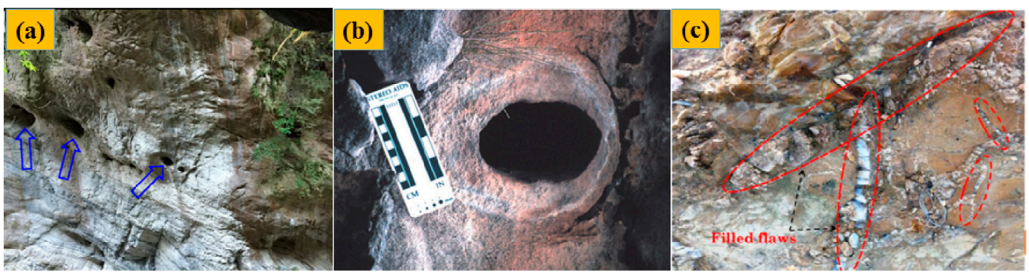

FIGURE 1
Rock mass with different types of defects in nature (Wray, 2009; Yang et al., 2017; Sharafisafa et al., 2019), **(A)** opening hole, **(B)** medium-sized tube and **(C)** filled flaws.

uniaxial compression process were then studied in detail based on energy theory, with particular attention paid to energy dissipation and instability processes under different hole depths. Subsequently, the strain field and crack patterns of the pre-drilled sandstone were primarily investigated using DIC technology. The evolution of microcracks was explored, and the mechanism of tensile and shear cracks was distinguished using RA and AF parameters. The complexity of the cracking processes was quantitatively assessed using multifractal theory.

2 Materials and methodology

2.1 Sample preparation

In this study, the test samples were sourced from a mine located in Chongqing. The particle diameter is between 0.25~0.35 mm, the bulk density is 2.48 g/cm^3, and the uniaxial compressive strength is 57.3 MPa. Initially, rock blocks with high integrity were selected and then transported to the laboratory for further processing. Adhering to the testing standards set by the International Society for Rock Mechanics (ISRM) (ISRM Testing Commission, 1978), the rock blocks underwent a series of preparatory procedures including drilling, cutting, and grinding. Finally, the rock samples were processed into rectangular specimens with dimensions of 30 mm in thickness, 80 mm in width, and 160 mm in height. At the center of each specimen, a cylindrical hole with a diameter of 10 mm was precision-drilled. In the subsequent, the hole was infilled with gypsum to simulate the complex internal composition and structure. The mechanical parameters of the infilling material include uniaxial compressive strength (53.17 MPa), tensile strength (3.61 MPa), elastic modulus (28.47 GPa), cohesion (0.15 GPa), internal friction angle (8.41°), and Poisson's ratio (0.13). To ensure the accuracy and reliability of the testing results, at least three samples with good homogeneity and no apparent surface cracks were chosen for each test. The geometry of the pre-drilled sandstone specimen is depicted in Figure 2.

2.2 Experimental setup and procedure

The experimental setup employed for this study featured an INSTRON material testing machine, a highly sophisticated apparatus equipped with a control panel, a loading unit, and a data acquisition unit. This machine is distinguished by its considerable loading capacity, which reaches up to 250 kN. The loading process was carefully controlled by displacement mode, with a constant loading rate of 0.05 mm/min to achieve a quasi-static loading condition. In order to monitor the development of microcracks within sandstone samples throughout the loading process, the experiment was conducted in conjunction with a PCI-II AE system. The AE sensors used in the experiment were of the Nano 30 model, characterized by a resonance frequency of 140 kHz and a sampling rate of 1 MHz. To mitigate the influence of environmental noise on the experimental outcomes, the AE system was calibrated with a threshold of 45 dB and a preamplifier setting of 40 dB. Additionally, to minimize signal attenuation and guarantee the faithful transmission of AE signals, Vaseline was applied as a coupling medium on the surface of the AE sensors. The DIC technique was utilized to capture the full field strain of pre-drilled sandstone samples. It is an optical non-contact testing technique consisting of a white LED light source and a camera. The successive images of the sample were monitored by Vic-Snap software at a frame rate of two digital images per second. The white matt paint is first evenly sprayed on the surface of the sample, and then black matte paint is sprayed on the white paint to form equidistant scattered spots. The principle of the DIC technique is the comparison of the reference speckle image and the deformed speckle image by identifying the degree of similarity of subsets series. The measurement accuracy of strain of this system is 0.002%. The configuration of the testing setup is illustrated in Figure 3.

3 Results and analysis

3.1 Mechanical property

3.1.1 Stress-time curves

To comprehensively analyze the mechanical behavior of rock samples throughout the entire loading process, the stress-time evolution for six representative groups of sandstone samples with varying drilling depths was examined, as shown in Figure 4. The stress-time curves depicted in Figure 4 reveal a distinct concave pattern during the initial loading phase, especially for samples with drilling depths of 5 mm and 10 mm. As the drilling depth increases, the peak stress demonstrates a steady decline, while the slopes of the six curves initially increase. The main reason for this phenomenon is that the compressive strength of the sandstone diminishes as the depth of the gypsum-infilled increases. Moreover, when the drilling depth is less than 10 mm, the mechanical properties of the samples with holes are relatively consistent with that of the intact sample. Its mechanical properties are almost not affected by infilling material. However, once the drilling depth is greater than 15 mm, the increasing depth further destroys the integrity of the rock's internal structure, which in turn makes it challenging for the gypsum infill to compensate for the lost load-bearing capacity. This results in a more pronounced deterioration in the mechanical performance of sandstone samples.

3.1.2 Peak strength

The peak strength of six groups of samples, each with different drilling depths, was plotted on a scatter diagram, as depicted in Figure 5. It can be found from Figure 5 that the peak strength of sandstone shows a linear downward trend with increasing drilling depth. Despite the fact that the infilling materials offer some degree of support at the interface with the matrix, they are unable to completely offset the weakening influence of the holes on the mechanical properties. As the drilling depth increases, the interface discontinuity and stress concentration are further exacerbated, leading to a progressive reduction in peak strength.

3.1.3 Strain field evolution

Figure 6 shows the evolution of the principal strain field in pre-drilled sandstone specimens under different depths. It is observed that the strain concentration zone on the specimen's surface predominantly occurs around the hole, consistently forming

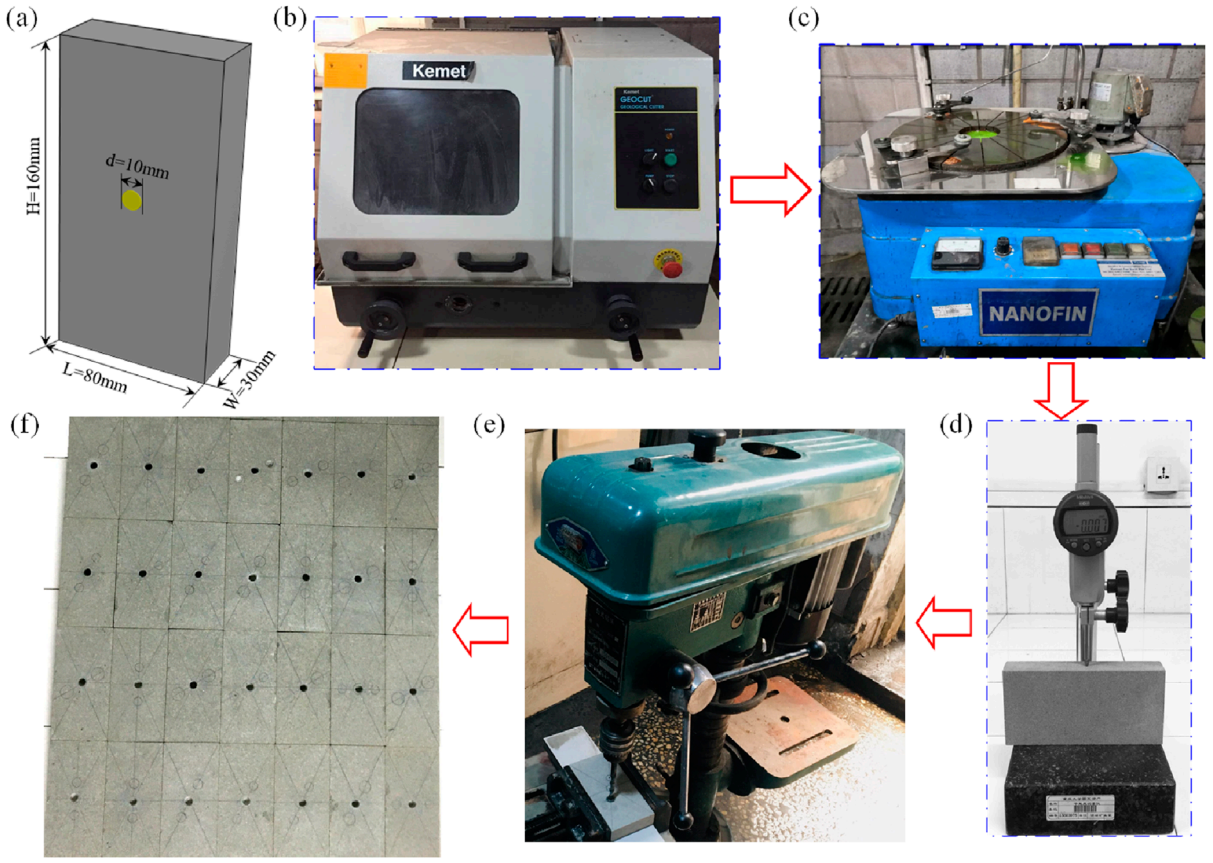

FIGURE 2
The geometry and processing of the pre-drilled sandstone specimen: **(A)** geometry, **(B)** high-precision cutting machine, **(C)** high-precision flat grinder, **(D)** flatness measuring instrument, **(E)** drilled machine and **(F)** drilled sandstone specimens.

a localized band of strain concentration, irrespective of the drilling depth. As the applied load increases, cracks initially emerge at the hole's perimeter and progressively spread circumferentially around it. In addition, when the stress level is greater than $0.8\sigma_c$, the speckle is accompanied by local shedding. This is mainly due to the strain experiencing a remarkable escalation, ultimately culminating in localized failure. In the strain field cloud, the high principal strain is depicted as elevated strain bands, which progressively expand and interpenetrate within the stress concentration zone.

For relatively shallow drilling depths, such as 5 mm and 10 mm, the principal strain field undergoes a gradual transformation during the loading process. The disturbance to the local stress field is minimal, and a localized strain concentration zone gradually forms at the hole's edge. This conclusion is similar to that of the intact specimen. The concentration zone remains largely confined to the vicinity of the hole, with no obvious penetration, and the damage degree is relatively low. Under the condition of medium drilling depths, such as 15 mm and 20 mm, the strain concentration band gradually formed in the early stage of loading, and the width and extent of the strain accumulation band gradually increase. The disturbance to the local stress field is more significant, and the high strain region around the hole gradually expands outward, and the crack develops gradually along the direction of the strain concentration zone, and finally forms a through-crack. For a 25 mm deeper hole that is close to the penetration depth, the strain concentration phenomenon becomes more remarkable. As the load increases, the width of the strain concentration band expands rapidly. Subsequently, the localized strain band extends throughout the entire specimen. Crack initiation occurs early, and the propagation speed is rapid. The influence of the hole on the whole stress field is most significant. When the load increases to the peak stress, the highlighted strain bands around the hole converge, forming macroscopic cracks and penetrating in multiple directions.

3.1.4 Coalescence pattern

By summarizing the coalescence modes of the pre-drilled sandstone at varying drilling depths, six representative specimens are identified, as depicted in Figure 7. Overall, with the increase of drilling depth, the failure mode of sandstone specimens gradually evolves from surface spalling to macroscopic crack coalescence, ultimately exhibiting highly intricate crack networks. In the case of shallow drilling depths (5 mm, 10 mm, and 15 mm), the specimens predominantly exhibit localized spalling failure around the holes, indicating that stress concentration is largely gathered around the hole, and the failure mode is relatively uniform. However, when the drilling depth reaches 20 mm, the failure mode shifts to a dominant crack originating from the upper left corner and extending to the lower right corner, accompanied by several branch cracks. As the

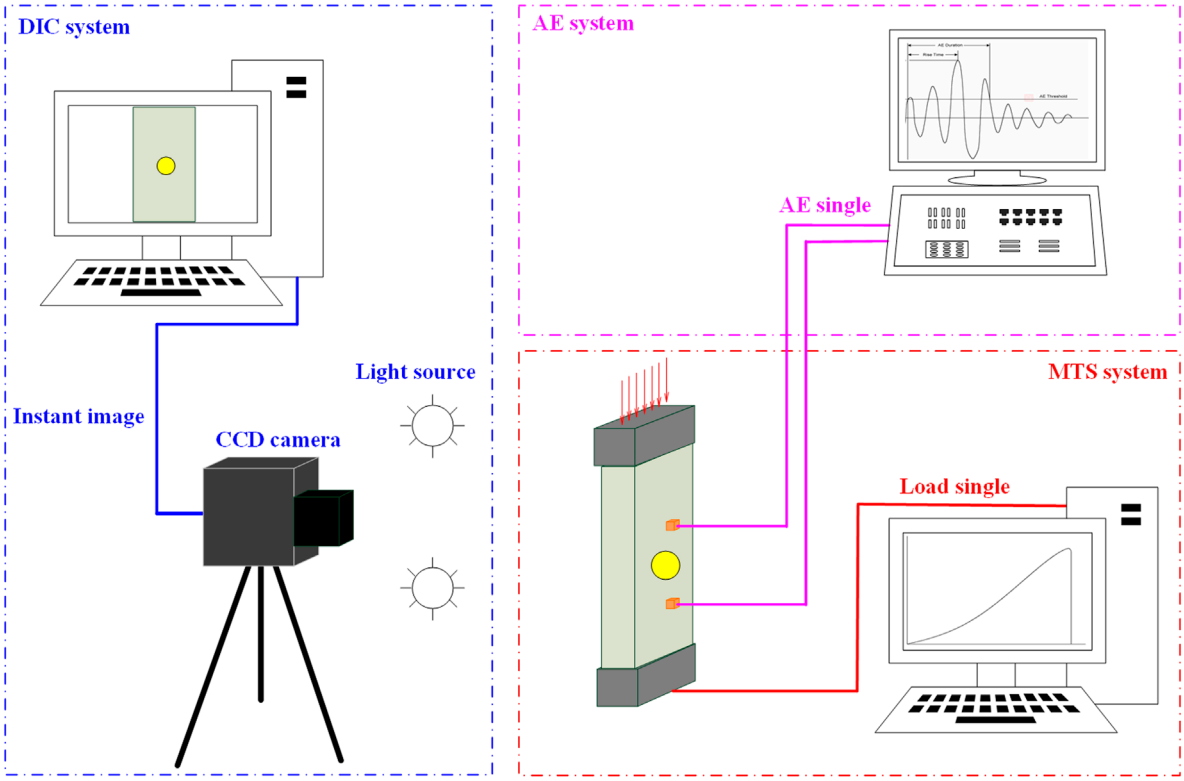

FIGURE 3
Testing apparatus.

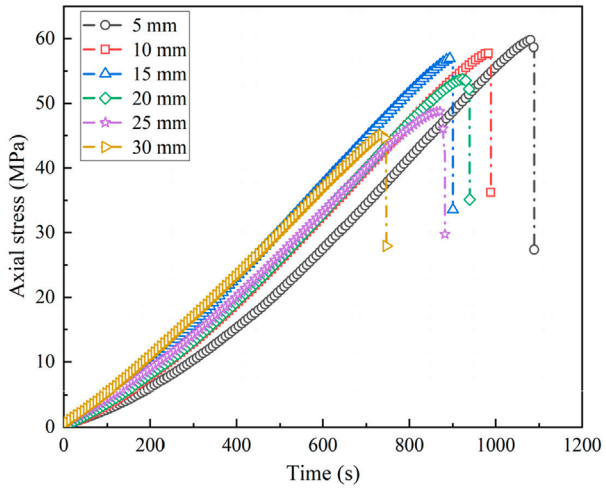

FIGURE 4
Axial stress-time curves of pre-drilled sandstone with different depths.

drilling depth is further increased to 25 mm, the failure mode transforms into a Y-shaped crack, signifying a more intricate stress field distribution around the hole, with the multidirectional crack expansion path reflecting local instability induced by the hole. At a depth of 30 mm, X-type cracks emerge in the specimen, and the complexity of the failure mode reached the highest. The cracks propagate in multiple directions, along with the generation of secondary cracks.

3.2 Energy evolution

3.2.1 Effect of drilling depth on strain energy

According to the laws of thermodynamics, the instability of rocks is essentially due to the input of external total energy. During the accumulation, dissipation, and release of various forms of energy within the rock, this is a process of mutual conversion of energy. Assuming that in a closed system, the total energy remains constant during energy conversion and energy transfer processes (Ding et al., 2023; Li P. et al., 2024). According to the first law of thermodynamics:

$$U = U_d + U_e \tag{1}$$

where U is the input mechanical energy, U_d is the elastic energy stored by the rock, and U_e is the dissipated energy generated by the plastic deformation and internal damage deformation of the rock.

Mechanical energy input by an external force to rock material:

$$E = \int_0^{\varepsilon} \sigma d\varepsilon \tag{2}$$

where σ is the axial stress, ε is the axial strain.

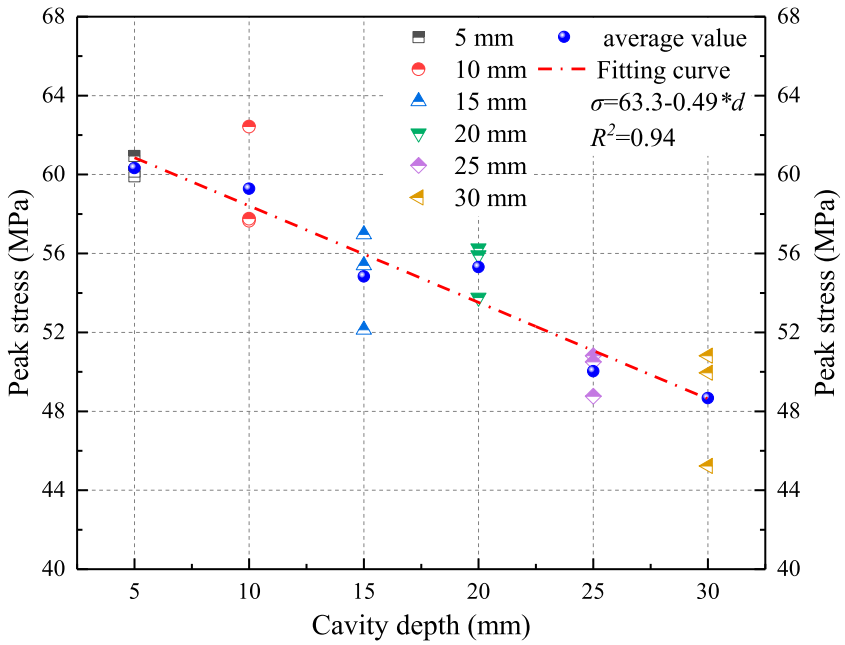

FIGURE 5
The peak stress of pre-drilled sandstone with different depths.

The elastic energy stored in rock material:

$$E_e = \frac{\sigma^2}{2E_0} \tag{3}$$

where E_0 is the elastic modulus.

The dissipated energy can be obtained from Equations 1–3:

$$U_d = \int_0^{\varepsilon} \sigma d\varepsilon - \frac{\sigma^2}{2E_0} \tag{4}$$

To investigate the energy-driven deformation mechanisms of sandstone with varying depths during loading, the total energy, elastic strain energy, and dissipated energy were calculated using Equations 1–4. Figure 8 illustrates the energy evolution of pre-drilled sandstone at different drilling depths under uniaxial compression. As depicted in Figure 8, the evolutionary trends for the total energy, elastic strain energy, and dissipated energy of the rock samples vary distinctly. The total energy exhibits a nonlinear ascending trend. During the initial loading phase, the dissipated energy rises gradually with increasing load, indicating minimal irreversible damage within the material. As loading progresses, the elastic energy surges nearly linearly as the peak stress is approached, suggesting that energy is predominantly stored in the form of elastic energy. In the post-peak stage, however, the elastic energy decreases abruptly, whereas the dissipated energy increases dramatically, signifying that the localized damage and crack initiation occur in sandstone. The majority of the energy is dissipated through irreversible crack growth, frictional sliding, and other deformation mechanisms. Initially, elastic energy predominates, but following peak stress, dissipative energy becomes the primary component of the energy distribution, delineating the transition from elastic deformation to plastic damage. Furthermore, the peak total energy decreases nonlinearly with increasing cavity depth, ranging from 29.81 kJ/m^3 at 5 mm to 22.65 kJ/m^3 at 30 mm. In contrast to the elastic strain energy, the peak dissipated energy increases with the depth of the infilled, from 4.49 kJ/m^3 at 5 mm to 6.25 kJ/m^3 at 30 mm, culminating in a sudden surge as the rock sample's load-bearing capacity is lost. This indicates that with deeper holes, crack propagation and irreversible damage intensify significantly during loading, highlighting the substantial increment in energy consumption associated with instability and failure processes. The stress concentration effect induced by deep holes exacerbates the initiation and propagation of cracks.

3.2.2 Effect of drilling depth on energy proportion

To gain a comprehensive understanding of the energy mechanism in pre-drilled sandstone specimens with varying drilling depths throughout the loading process, a quantitative examination of the proportional correlation between elastic strain energy and dissipated energy is essential. Figure 9 presents the proportions of elastic strain energy and dissipated energy for pre-drilled sandstone samples with different drilling depths.

At the onset of loading, the closure of internal defects leads to the dissipation of a portion of the energy during the crack closure phase, thereby increasing the ratio of dissipated energy. In Stage I, the dissipated energy rises nonlinearly with the increment of deformation, and it exceeds the elastic energy, predominantly due to the closure and friction within the micro-cracks of the sandstone. During Stage II, the micro-cracks and pre-existing pores in sandstone are completely closed, and the proportion of dissipated energy gradually decreases with the progression of deformation. At the same time, a fraction of the total energy continues to be stored as elastic energy, indicating that less damage occurs in the sample. In Stage III, the proportion of dissipated energy increases, whereas the

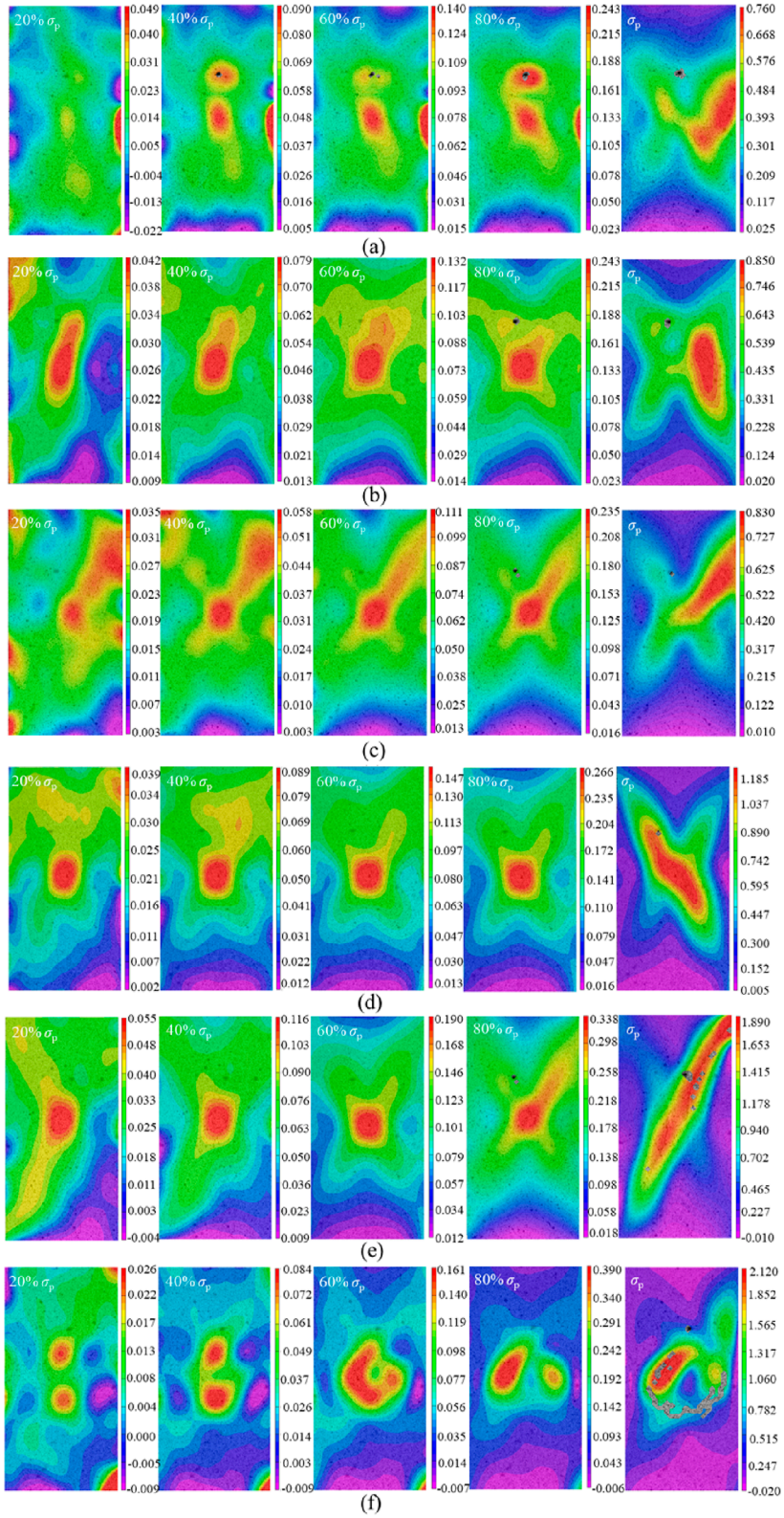

FIGURE 6
Evolution of principal strain of sandstone infilling with different depths: **(A)** 5 mm, **(B)** 10 mm, **(C)** 15 mm, **(D)** 20 mm, **(E)** 25 mm, and **(F)** 30 mm.

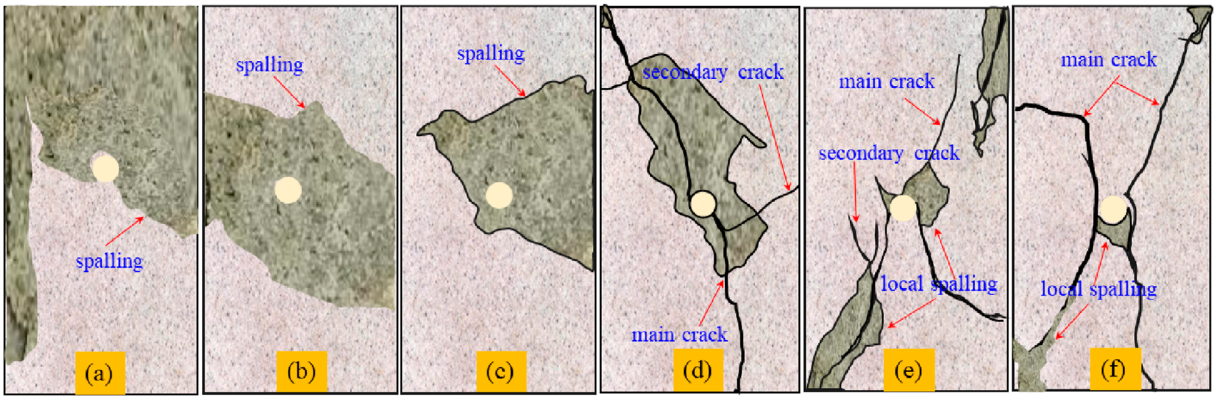

FIGURE 7
Coalescence modes of the pre-drilled sandstone with different depths: **(A)** 5 mm, **(B)** 10 mm, **(C)** 15 mm, **(D)** 20 mm, **(E)** 25 mm, and **(F)** 30 mm.

proportion of elastic energy experiences a sharp reduction. This is mainly due to the limited number of micro-cracks in sample leading to the release of the mechanical energy as dissipated energy. Upon reaching peak strength, the rock transits into the macroscopic failure stage. Consequently, the dissipated energy increases dramatically, whereas the elastic energy decreases sharply. This is attributed to the propagation and coalescence of cracks within the sandstone, leading to a reduction in load-bearing capacity and the rapid conversion of the stored elastic energy into dissipated energy, showing a steep upward trend in the dissipated energy curve.

3.3 Cracking processes

3.3.1 AE characteristics

The presence of micro-cracks and voids within the rock matrix may undergo closure or opening under loading conditions. The elastic waves emitted as a result of these changes are captured as AE signals, which provide insight into the fracturing process of rock materials (Lei et al., 2020; Tian et al., 2023; Wang et al., 2021). AE signals are capable of characterizing a series of processes such as the initiation, propagation, and coalescence of micro-cracks in rocks. Figure 10 shows the AE count-stress curves over time for sandstone samples with varying drilling depths. By analyzing the AE characteristics throughout the deformation and failure, the entire loading process can be categorized into four distinct stages: the micro-crack compaction stage, the micro-crack initiation and propagation stage, the macro-crack development stage, and the pre-peak fracture stage.

Firstly, in the micro-crack compaction stage, AE events were detected in all six groups of samples with different drilling depths. This is because the micro-pores and cracks within the rock samples are being compacted. However, as the drilling depth increases, the captured cumulative AE signals show a significant downward trend. The stress-time curves generally show a steady rise or a slightly concave trend, which is likely due to the discrete AE events generated by the micro-cracks and voids within the rock samples. Secondly, in the micro-crack initiation and propagation stage, the number of AE signals decreases with the increasing depth of the drilling pores, but the number of high-energy reflection events increases. This is because after the micro-cracks are compacted, new micro-cracks begin to form and propagate, resulting in the capture of high-amplitude energy signals. The cumulative energy curve also begins to show a stepped-up trend, mainly because the matrix particles and cracks within the rock samples, are gradually compacted, leading to the formation of internal micro-cracks. The subsequent is the macro-crack development stage, characterized by an increasing density of AE signals within samples. The AE energy characteristics indicate that larger amplitude energy signals are captured during the stable development of cracks. The slope of the cumulative energy curve increases more significantly than in the previous stage. With the increase of drilling depth, the cumulative AE energy gradually increases, and the clustering phenomenon of the energy curve becomes more pronounced, transforming from a stepped-up rise to a steeper one. Finally, there is the pre-peak stage, which occurs almost simultaneously with or just before the fracturing of the sample. The density of AE signals increases sharply and lasts for the shortest duration, confirming that the sandstone material is a typical quasi-brittle material. Meanwhile, both the AE energy curve and the cumulative energy curve rise sharply, while the stress-time curve shows a sudden drop. For samples with different drilling depths, a significant release of energy is observed within the rock samples before fracturing. As the drilling depth increases, the phenomenon of crack penetration becomes more evident. From the cumulative AE energy curve, it can be inferred that as the depth of the cavity increases, the total AE energy produced during the entire loading process gradually decreases.

3.3.2 Microcrack evolution

It is well-known that when rocks are subjected to external load, they may produce tensile cracks, shear cracks, or a combination of tensile-shear cracks. When different types of micro-cracks are formed, rocks can generate AE signals with different waveform characteristics. As micro-cracks accumulate to a certain extent, they can form macroscopic cracks. Therefore, the study of the evolution of micro-cracks is very important for revealing the macroscopic fracturing of sandstone. To characterize the evolution of micro-cracks during the deformation and failure of the rock,

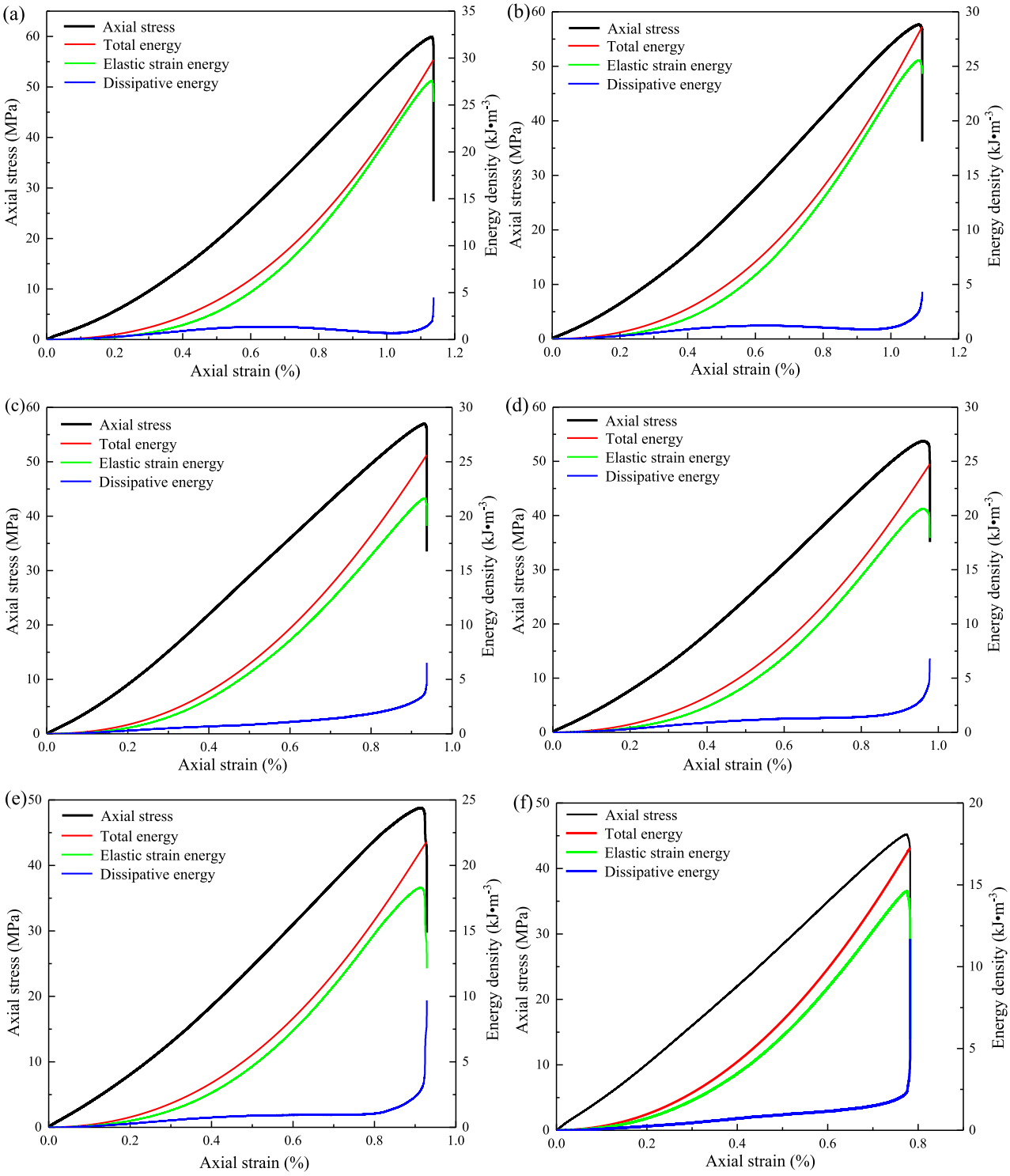

FIGURE 8
Energy evolution of pre-drilled sandstone with different depths: **(A)** 5 mm, **(B)** 10 mm, **(C)** 15 mm, **(D)** 20 mm, **(E)** 25 mm, and **(F)** 30 mm.

indirect AE parameters are obtained by calculating the relationships between parameters such as AE count, duration time, rise time, and amplitude, such as AF and RA (Bi et al., 2024).

$$AF = \frac{C}{D_T} \tag{5}$$

where AF is the average frequency of the AE signal, C is the AE count, and D_T is the duration time.

$$RA = \frac{R_T}{A} \tag{6}$$

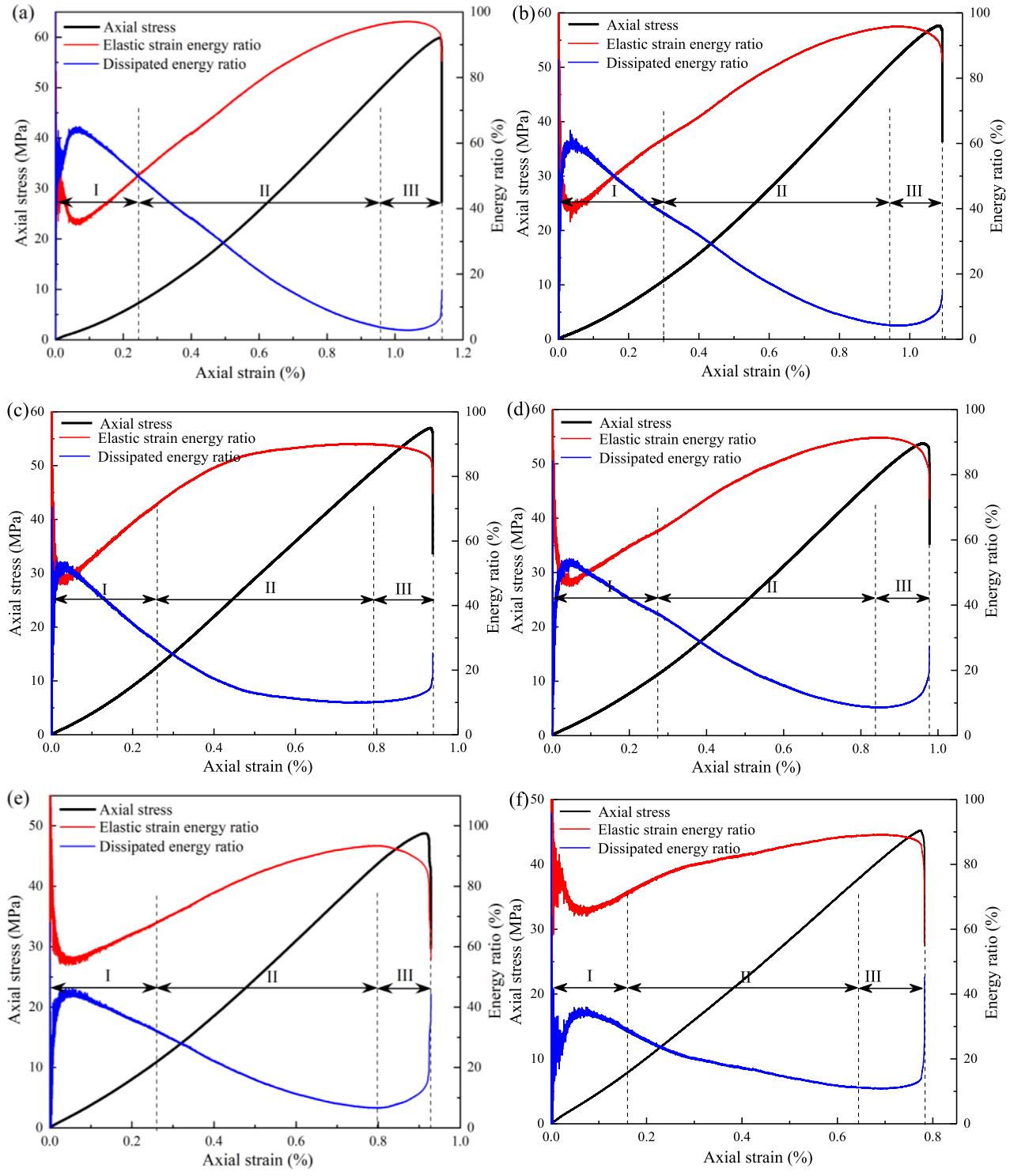

FIGURE 9
Proportions of elastic strain energy and dissipated energy of pre-drilled sandstone with different depths: **(A)** 5 mm, **(B)** 10 mm, **(C)** 15 mm, **(D)** 20 mm, **(E)** 25 mm, and **(F)** 30 mm.

where RA is the ratio of the rise time to amplitude, R_T is the rise time, and A is the amplitude.

Previous research has demonstrated that indirect AE parameters are obtained from Equations 7–13, which can be utilized to qualitatively determine the type of micro-cracks (Li et al., 2022; Lei et al., 2023a; Lei et al., 2023b; Wang et al., 2024b; Wang H. et al., 2024). Specifically, the characteristics of micro-cracks can be inferred as follows: A relatively low RA value coupled with a high

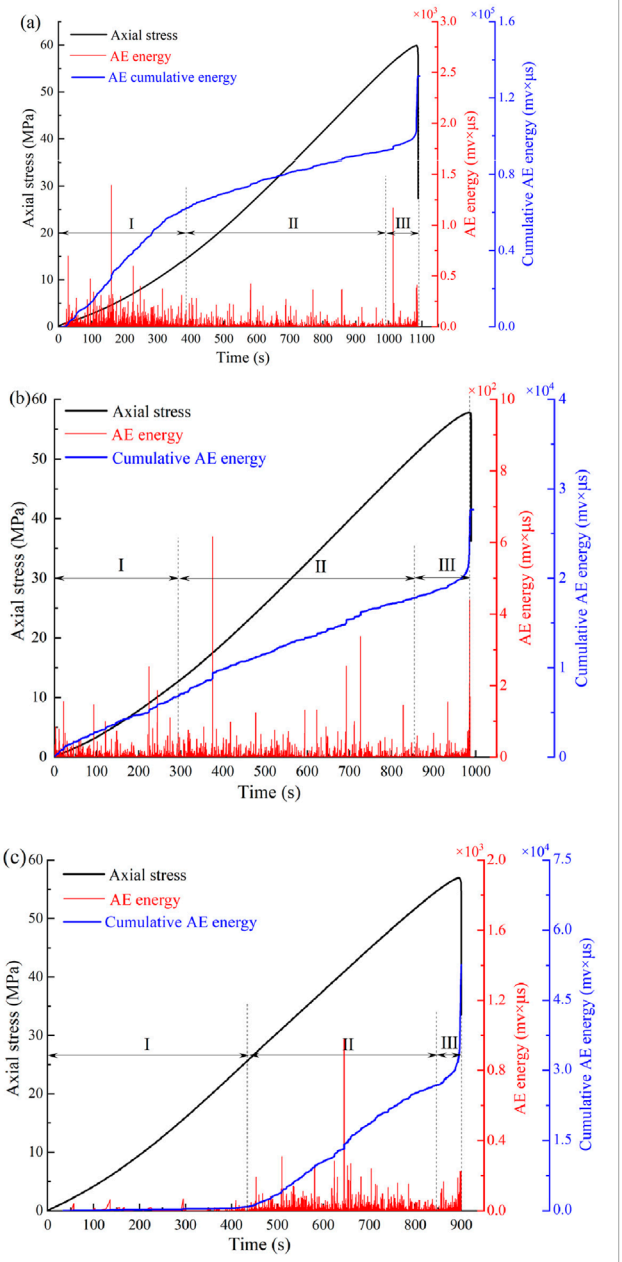

FIGURE 10
(Continued).

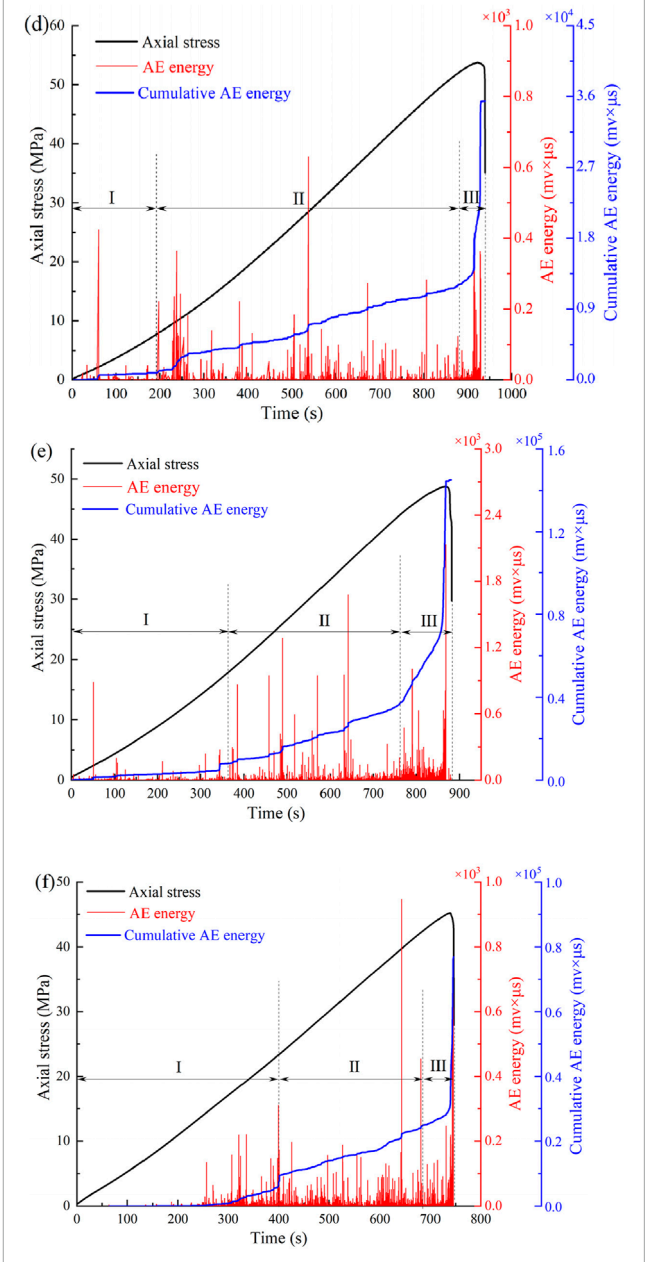

FIGURE 10
(Continued). Evolution of axial stress and AE energy of pre-drilled sandstone with different depths: **(A)** 5 mm, **(B)** 10 mm, **(C)** 15 mm, **(D)** 20 mm, **(E)** 25 mm, and **(F)** 30 mm.

average frequency AF value indicates that the failure is primarily due to tensile cracks. Conversely, a high RA value along with a low AF value suggests that the failure is predominantly by shear cracks. When both RA and AF values are low, it indicates a mixture of tensile-shear cracks. Many researchers have agreed that a diagonal line can serve as a discriminator between tensile and shear cracks on an RA-AF plot (Zhang and Zhou, 2023; Niu et al., 2023; Xiao et al., 2023; Gu et al., 2024). The area above the dividing line is associated with tensile failure, while the area below the line is indicative of shear failure. Moreover, the slope of the dividing line, which is the AF/RA ratio, is considered a critical threshold for distinguishing between the two types of failures. The traditional method takes the diagonal line of RA/AF as the dividing line. Also, Du et al. (2020) found that the dividing line of different types of rocks is different, and its experiment found that the slope of the dividing line of sandstone is about 1/70. Niu et al. (2020) used the kernel density estimation (KDE) function to divide the high-density region of RA and AF values in crack classification, and the results showed that the ratio of RA/RF was 1/70, which was a reasonable proportion. This study adopts this threshold to characterize the evolution law of micro-cracks during compression testing.

By using this threshold, researchers can categorize the micro-crack behavior observed during the test into tensile, shear, or

a combination of both, thus providing insights into the failure mechanisms at play within the rock material under compression. This approach allows for a more detailed understanding of how micro-cracks develop and propagate, which is crucial for predicting the stability and behavior of rock structures in various engineering applications. To elucidate the characteristics of micro-cracks, the relationship between the crack classification parameters RA and AF was determined using statistical calculation methods. Subsequently, the probability density cloud of RA-AF was generated with the built-in probability density function. Figure 11 shows the RA-AF spectrum diagram of micro-crack evolution for pre-drilled sandstone samples with varying depths. It can be found that the micro-crack evolution differs among sandstone samples with different drilling depths. For samples with a drilling depth of 5 mm–10 mm, the probability density is predominantly concentrated in areas of low RA and low AF values, as well as low RA and higher AF values. This indicates that the failure mechanism in these sandstone samples is mainly a combination of tensile and shear failures, with both modes of failure coexisting.

In samples with filling fracture depths of 15 mm–20 mm, the probability density is mainly focused in the low RA and low AF value area, suggesting that the crack failure mechanism is primarily tensile-shear mixed failure. However, there is also a small distribution in the low RA and high AF value area, indicating that tensile crack failure accounts for a minor proportion. For samples with a filling depth of 25 mm–30 mm, the probability density is mainly distributed in the low RA and low AF value, as well as the high RA and low AF value. This is mainly a mixed tensile-shear and shear failure. As the depth of the filled pore increases, the distribution of indirect AE parameters in the low RA and high AF value area of the sandstone shows a gradual increasing trend. This suggests that shear cracks are progressively becoming more prevalent. Shear cracks constitute a significant proportion, with the shear failure mode being dominant. The increased filling depth enhances the effect of stress concentration within the rock, making it easier for local areas to reach the shear strength of the sandstone and thereby promoting the generation of shear cracks. The presence of deep holes intensifies the constraint on the surrounding materials, and this high constraint is more conducive to shear slip phenomena. Additionally, the increased drilling depth alters the stress field distribution around the hole, causing shear forces to act more deeply within the rock, forming a failure zone primarily influenced by shear stress. With regard to deeper holes, shear cracks become the primary pathway for energy release, thereby fostering the generation of shear cracks. Furthermore, the potential non-uniform deformation of deep holes further complicates the local stress field and is favorable for the development of shear cracks. Consequently, as the drilling depth increases, the proportion of shear cracks in the overall crack population rises.

3.3.3 Multi-spectral characteristics

The fractal theory is widely used in geophysics to study the deformation and failure of rocks, which describes the irregular phenomenon in nature (Liu et al., 2019; Li et al., 2021; Liu X. G. et al., 2021; Sun et al., 2022). In this study, the box-covering method is employed to calculate the probability distribution of AE activities. First, define the AE time series $\{x(i); i = 1, 2, 3, \ldots A\}$, and then divide it into consecutive N equal parts, each part is L in length. The normalized probability of each interval is defined as:

$$P_i = \frac{S_i}{\sum_{i=1}^{N} S_i}, i = 1, 2, \cdots N \tag{7}$$

where P_i indicates the normalized probability density, and S_i represents the cumulative sum of the ith interval.

The partition function is defined as:

$$X(q, L) = \sum_{i=1}^{N} P_i^q \tag{8}$$

where q indicates the order of statistical moment, and L represents the scale length.

For different q values, the relationship between the partition function and L is given as:

$$X(q, L) \propto L^{\delta(q)} \tag{9}$$

By constantly changing the scale length m and repeating calculation, the Hurst exponent $\delta(q)$ can be obtained by taking the slope of the double logarithmic function from the fitting curves of ln $(X\ (q, L))$ and ln(M).

The single parameter cluster $\mu_i(q, M)$ of normalized measures is defined as:

$$\mu_i(q, M) = \frac{[P_i(L)]^q}{\sum_{j=1}^{N} [P_i(L)]^q} \tag{10}$$

where $P_i(L)$ is the probability distribution function, and j is the number of times the power-weighted processing is performed with q fixed.

After Legendre transformation, fractal spectrum function $f(q)$ and average singularity $\alpha(q)$ can be given as:

$$f(q) = -\lim_{N\to\infty} \frac{1}{\ln N} \sum_{i=1}^{N} \mu_i(q, L) \ln [\mu_i(q, L)] \tag{11}$$

$$\alpha(q) = -\lim_{N\to\infty} \frac{1}{\ln N} \sum_{i=1}^{N} \mu_i(q, L) \ln [P_i(L)] \tag{12}$$

The spectrum width $\triangle\alpha$ is:

$$\Delta\alpha = \alpha_{max} - \alpha_{\min} \tag{13}$$

where $\alpha_{\max}$ is the maximum value of the singularity index, $\alpha_{\min}$ is minimum of the singularity index.

To delve into the crack characteristics throughout the deformation and fracturing of rock samples, AE signals were analyzed based on Equations 7–13. Figure 12 shows the multifractal spectrum characteristics of the AE energy parameters for pre-drilled sandstone samples with three typical drilling depths. As observed in Figure 12, the pre-drilled sandstone samples show evident spectrum characteristics, suggesting that the AE signals emitted during the loading deformation process exhibit pronounced nonlinear characteristics. Furthermore, the occurrence probability of signals with smaller amplitudes is higher than those of larger ones, indicating that the rock samples undergo an intricate process of damage and fracturing processes with regard to the initiation, propagation, and expansion of microcracks. The scale of crack fracturing can be quantitatively assessed through AE signals. The higher amplitude signals imply larger-scale internal deformation and fracturing, whereas lower amplitude signals suggest

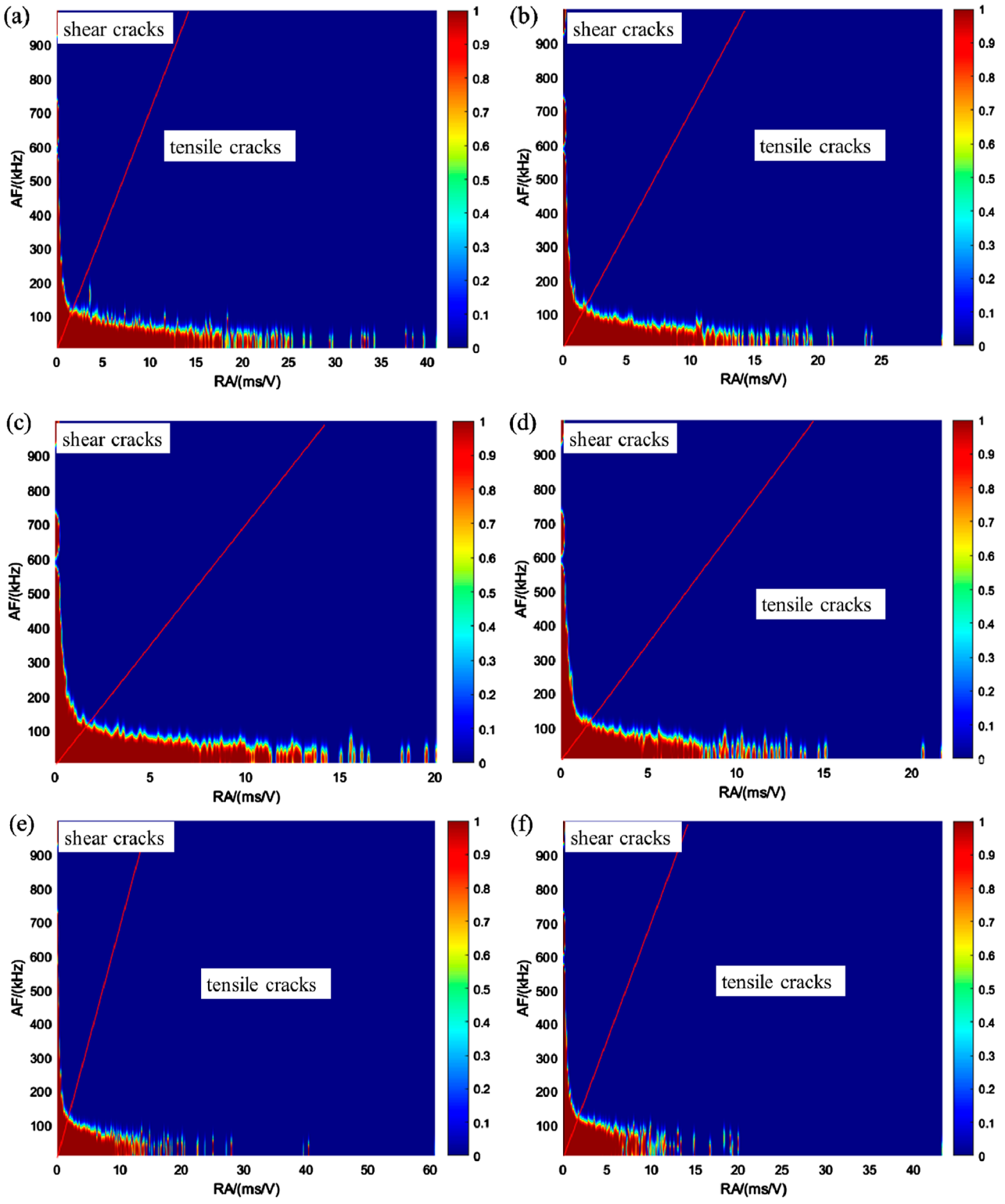

FIGURE 11
Evolution of microcracks of pre-drilled sandstone containing different depths: **(A)** 5 mm, **(B)** 10 mm, **(C)** 15 mm, **(D)** 20 mm, **(E)** 25 mm, and **(F)** 30 mm.

smaller-scale fractures. The spectrum features also enable the differentiation of the structural variations within AE signals. It is noted that as the drilling depth increases, the width of the multifractal spectrum expands. The decrease of the spectrum width indicates that the singularity intensity distribution of AE signals becomes more concentrated and the complexity decreases.

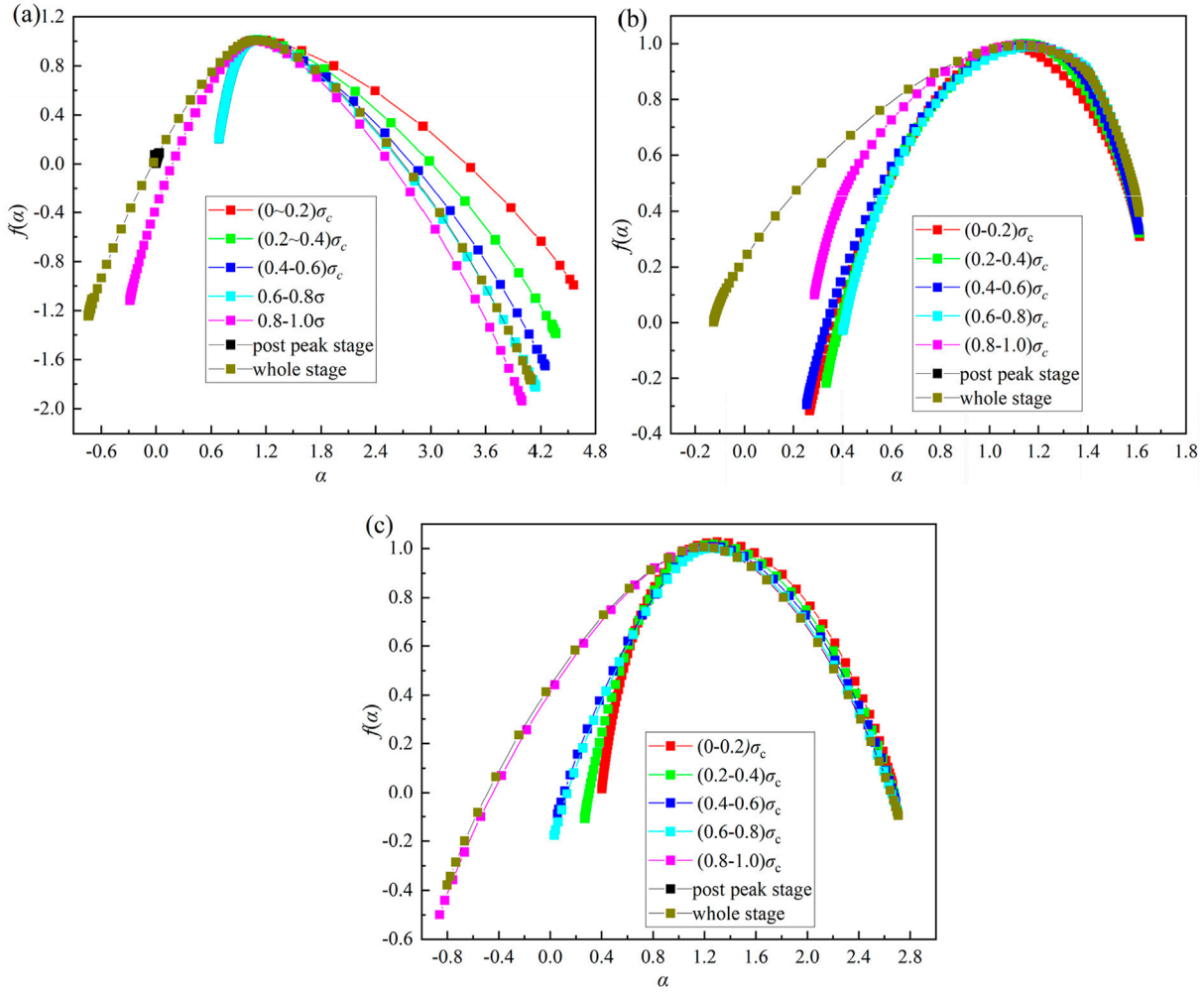

FIGURE 12
Multi-spectral spectrum of pre-drilled sandstone with typical depths: **(A)** 5 mm, **(B)** 15 mm, and **(C)** 30 mm.

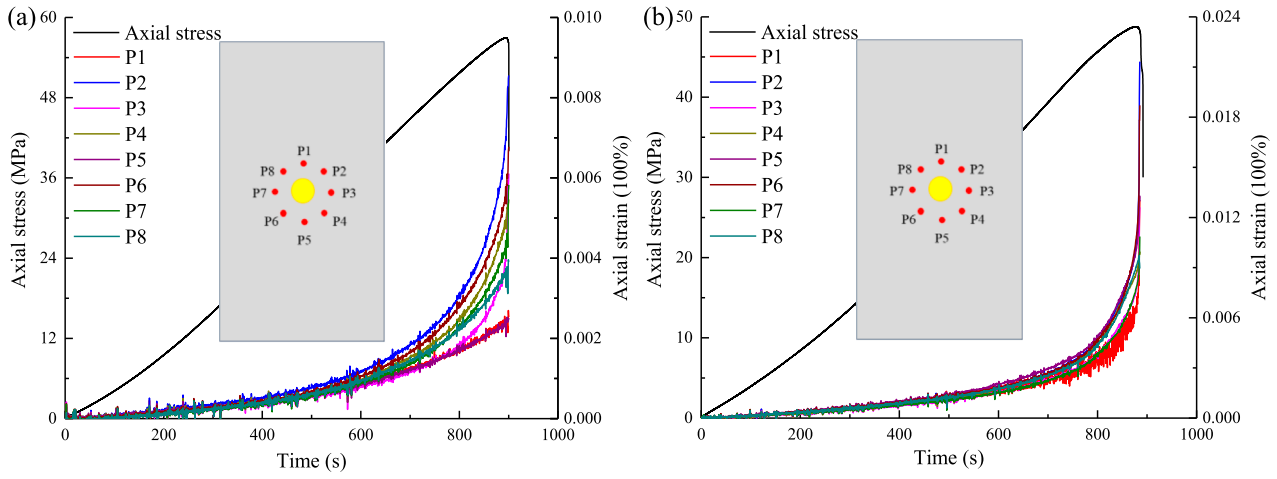

FIGURE 13
Strain evolution at monitoring points in pre-drilled sandstone with typical depths: **(A)** 15 mm and **(B)** 25 mm.

The results show that the cracks change from multi-scale random distribution to larger scale single-mechanism failure mode, that is, AE events in the sample are mainly caused by large-scale shear slip. In cases with shallower hole, such as a pore depth of 5 mm, the contribution of micro cracks and slippage between less disturbed mineral particles results in a narrower multifractal spectrum (with $\Delta\alpha$ approximately 4.33). However, when the depth reaches 30 mm, the spectrum width narrows to 3.20, and the AE signal exhibits a richer frequency spectrum. The deeper gypsum infilling promotes the creation of new cracks and active dislocation slips, offering multiple avenues for stress release and thus widening the spectral width. The damping properties of the gypsum material itself partially restrain the development of large-scale cracks, leading to a slight increment in frequency measurement subset (Δf), ranging between −0.42 and 0.23. Moreover, the gypsum infilling alters the material consistency of the rock, thereby influencing the propagation path and velocity of stress waves, mitigating stress concentration at crack tips, and reducing the incidence of large-scale cracks (Ma et al., 2025).

4 Discussion

To further elucidate the deformation and fracture mechanism of pre-drilled sandstone, two representative samples with drilling depths of 15 mm and 25 mm were chosen for study. Monitoring points were strategically positioned around the holes to monitor the strain variations throughout the entire loading process. Eight such monitoring points were arranged 20 mm away from the center of the hole in a clockwise direction. The strain progression at these various points around the hole is depicted in Figure 13. A careful examination of Figure 13 reveals that the strain values progressively increase with the applied load. Notably, the cumulative strains recorded at points P2 and P6 are substantially greater than those at the other monitoring points. This observation can be attributed to the pronounced tensile forces acting on the sides of the cavity during loading, leading to stress concentration in these areas. Unlike the load transfer that occurs above and below the hole, the regions flanking the hole experience a higher degree of tensile force, resulting in the primary locations for crack initiation.

In addition, for the sample with a drilling depth of 15 mm, a notable strain discrepancy was observed at each monitoring point during the initial loading phase. In contrast, the sample containing a drilling depth of 25 mm displayed a pronounced strain difference when approaching the peak stress. Given its brittle nature, sandstone is susceptible to crack propagation in areas of stress concentration. The plastic properties of the infill materials, however, offer a degree of stress buffering in the early stages of loading (Wu et al., 2024). For the 15 mm shallow sample, the infilling was insufficient to counteract the internal stresses within the cavity, promoting stress concentration in the surrounding area. Consequently, during the initial loading phase, a distinct strain difference among the monitoring points was already apparent.

In the case of the 25 mm drilling depth sample, the material effectively distributed the stress around the hole, leading to a more uniform stress distribution at the outset and no discernible strain differences across the monitoring points. However, as loading progressed, particularly approaching peak stress, the plastic deformation or localized failure of the gypsum infill caused a re-concentration of stress, resulting in a marked increase in strain differences. Furthermore, the progressive damage and microcrack propagation around the hole during loading exacerbated the cumulative strain effect, especially at points P2 and P6, where stress concentration was most significant. Crack propagation at these points accelerated the growth of strain. For sample with a drilling depth of 15 mm, the insufficient infill depth precipitated early crack propagation, leading to a significant initial strain discrepancy. For sample with a drilling depth of 25 mm, however, the stress-relieving effect of the gypsum infilling was not evident in strain differences until the sample was near its peak stress.

5 Conclusion

(1) With the increase of the drilling depth, the peak strength of the sample decreases linearly. In addition, the failure mode of the sandstone evolves from localized spalling around the holes to complex crack networks. When the depth is relatively shallow, the failure of the sample tends to be surface spalling, whereas deeper holes promote a multi-crack propagation pattern, indicating the rock structure shows an obvious weakening phenomenon.

(2) DIC observation shows that the major principal strain concentration area mainly appears around the hole, forming a local strain concentration area. As the applied load is incremented, the initiation of cracks is observed to commence at the periphery of the hole.

(3) In the case of samples with shallower drilling depth, the AE signal exhibits higher frequencies, which are typically associated with large-scale fracturing events. In the case of samples with deeper holes, the density of AE signals decreases, suggesting fewer but more significant fracturing events. Additionally, the spectrum of AE signals becomes broader. This widening of the AE signal spectrum is indicative of an increase in the heterogeneity and the extent of dislocation slip occurring between mineral particles within the rock matrix.

Data availability statement

The original contributions presented in the study are included in the article/supplementary material, further inquiries can be directed to the corresponding author.

Author contributions

JL: Methodology, Software, Writing–original draft. RL: Investigation, Supervision, Writing–review and editing.

Funding

The author(s) declare that financial support was received for the research, authorship, and/or publication of this article. Hubei Key Laboratory of Disaster Prevention and Mitigation (China Three Gorges University) (No. 2023KJZ18).

Conflict of interest

The authors declare that the research was conducted in the absence of any commercial or financial relationships that could be construed as a potential conflict of interest.

Generative AI statement

The author(s) declare that no Generative AI was used in the creation of this manuscript.

Publisher's note

All claims expressed in this article are solely those of the authors and do not necessarily represent those of their affiliated organizations, or those of the publisher, the editors and the reviewers. Any product that may be evaluated in this article, or claim that may be made by its manufacturer, is not guaranteed or endorsed by the publisher.

References

Bi, J., Zhao, Y., Wu, Z. J., Li, J. S., and Wang, C. L. (2024). Research on crack classification method and failure precursor index based on RA-AF value of brittle rock. *Theor. Appl. Fract. Mech.* 129, 104179–179. doi:10.1016/j.tafmec.2023.104179

Chen, J., Ye, Y. B., Pu, Y. Y., Xu, W. H., and Deren, M. L. (2022). Experimental study on uniaxial compression failure modes and acoustic emission characteristics of fissured sandstone under water saturation. *Theor. Appl. Fract. Mech.* 119, 103359–359. doi:10.1016/j.tafmec.2022.103359

Ding, S., Tang, S. B., Jia, H. L., and Li, Y. B. (2023). The influence of water on the failure characteristics of sandstone under uniaxial compression conditions by acoustic emission and NMR observation. *Eng. Geol.* 322, 107173–173. doi:10.1016/j.enggeo.2023.107173

Dong, J. L., Gao, Y. T., Wu, T. H., Huang, C. F., Li, J. W., and Zhou, Y. (2024). Failure behaviour of various rocks coated new thin spray-on liner with different curing time under uniaxial compression: insights from AE and DIC. *Constr. Build. Mater.* 449, 138515–515. doi:10.1016/j.conbuildmat.2024.138515

Dong, L. J., Zhang, Y. H., Bi, S. J., Ma, J., Yan, Y. H., and Cao, H. (2023). Uncertainty investigation for the classification of rock micro-fracture types using acoustic emission parameters. *Int. J. Rock Mech. Min. Sci.* 162, 105292–292. doi:10.1016/j.ijrmms.2022.105292

Du, K., Li, X. F., Tao, M., and Wang, S. F. (2020). Experimental study on acoustic emission (AE) characteristics and crack classification during rock fracture in several basic lab tests. *Int. J. Rock Mech. Min. Sci.* 133, 104411–411. doi:10.1016/j.ijrmms.2020.104411

Du, K., Sun, Y., Zhou, J., Manoj, K., and Gong, F. Q. (2022). Mineral composition and grain size effects on the fracture and acoustic emission (AE) characteristics of rocks under compressive and tensile stress. *Rock Mech. Rock Eng.* 55 (10), 6445–6474. doi:10.1007/s00603-022-02980-y

Du, Y. T., Li, T. C., Wang, B. X., Zhang, S. L., Li, H., Zhang, H., et al. (2023). Experimental study on mechanical characteristics and permeability evolution during the coupled hydromechanical failure of sandstone containing a filled fissure. *Acta Geotech.* 18 (8), 4055–4075. doi:10.1007/s11440-023-01816-5

Feng, W. L., Qiao, C. S. ;, Niu, S. J., Yang, Z., and Wang, T. (2020). An improved nonlinear damage model of rocks considering initial damage and damage evolution. *Int. J. Damage Mech.* 29 (7), 1117–1137. doi:10.1177/1056789520909531

Gao, D., Peng, J., Kwok, F. C. Y., Wang, H. L., and Wang, L. F. (2024). Influence of intermediate principal stress on mechanical and failure properties of anisotropic sandstone. *Rock Mech. Rock Eng.* 57, 7795–7812. doi:10.1007/s00603-024-03986-4

Gu, C., Sun, Q., Geng, J. S., Zhang, Y. L., and Jia, H. L. (2024). Acoustic emission real-time monitoring and analysis of microwave thermal damage of granite. *Environ. Earth Sci.* 83 (15), 443. doi:10.1007/s12665-024-11745-5

Hebert, J., and Khonsari, M. (2023). The application of digital image correlation (DIC) in fatigue experimentation: a review. *Fatigue and Fract. Eng. Mater. and Struct.* 46 (4), 1256–1299. doi:10.1111/ffe.13931

Hu, X. J., Gong, X. N., Hu, H. B., Guo, P. P., and Ma, J. J. (2022). Cracking behavior and acoustic emission characteristics of heterogeneous granite with double pre-existing filled flaws and a circular hole under uniaxial compression: insights from grain-based discrete element method modeling. *Bull. Eng. Geol. Environ.* 81 (4), 162. doi:10.1007/s10064-022-02665-4

Huang, Y. H., Wu, S. Y., and Yang, C. (2024). Experimental study on the failure behaviors of sandstone specimens with two fissures under triaxial loading and unloading conditions. *Eng. Fract. Mech.* 298, 109933. doi:10.1016/j.engfracmech.2024.109933

ISRM Testing Commission (1978). Suggested method for determining tensile strength of rock materials. *Int. J. Rock Mech. Min. Sci. Geomechanics Abstr.* 15 (3), 99–103. doi:10.1016/0148-9062(78)90003-7

Lei, R. D., Filippo, B., Hu, C., Lu, Z. H., and Yan, X. F. (2023b). Early-warning signal recognition methods in flawed sandstone subjected to uniaxial compression. *Fatigue and Fract. Eng. Mater. and Struct.* 46 (3), 955–974. doi:10.1111/ffe.13911

Lei, R. D., Tan, Y. L., Filippo, B., Hu, C., and Qi, X. (2023a). Temporal-frequency distribution and multi-fractal characterization of acoustic emission of rock materials containing two parallel pre-existing flaws. *Fatigue and Fract. Eng. Mater. and Struct.* 46 (6), 2139–2155. doi:10.1111/ffe.13988

Lei, R. D., Zhang, Z. Y., Filippo, B., Ranjith, P. G., and Liu, L. (2020). Cracking process and acoustic emission characteristics of sandstone with two parallel filled-flaws under biaxial compression. *Eng. Fract. Mech.* 237, 107–253. doi:10.1016/j.engfracmech.2020.107253

Li, K. S., Luan, Y. Q., Zhang, J. P., and Liu, C. X. (2024). Experimental study on mechanical behavior, AE response and energy evolution of fissure-filled sandstone from mine roadway under conventional triaxial compression. *Theor. Appl. Fract. Mech.* 130, 104334–334. doi:10.1016/j.tafmec.2024.104334

Li, P., Cai, M. F., Gao, Y. B., Gorjian, M., Miao, S. J., and Wang, Y. (2022). Macro/mesofracture and instability behaviors of jointed rocks containing a cavity under uniaxial compression using AE and DIC techniques. *Theor. Appl. Fract. Mech.* 122, 103620. doi:10.1016/j.tafmec.2022.103620

Li, P., Liu, Y., Cai, M. F., Miao, S. J., Dai, L. P., and Gorjian, M. (2024). Accurate stress measurement using hydraulic fracturing in deep low-permeability reservoirs: challenges and research directions. *Adv. Geo-Energy Res.* 14 (3), 165–169. doi:10.46690/ager.2024.12.02

Li, X. L., Chen, S. J., Liu, S. M., and Li, Z. H. (2021). AE waveform characteristics of rock mass under uniaxial loading based on Hilbert-Huang transform. *J. Cent. South Univ.* 28 (6), 1843–1856. doi:10.1007/s11771-021-4734-6

Liu, J., Li, Q. P., Wang, X. R., Wang, Z. Q., Lu, S. P., Sa, Z. Y., et al. (2022b). Dynamic multifractal characteristics of acoustic emission about composite coal-rock samples with different strength rock. *Chaos, Solit. and Fractals* 164, 112725–725. doi:10.1016/j.chaos.2022.112725

Liu, S. M., Li, X. L., Li, Z. H., Chen, P., Yang, X. L., and Liu, Y. J. (2019). Energy distribution and fractal characterization of acoustic emission (AE) during coal deformation and fracturing. *Measurement* 136, 122–131. doi:10.1016/j.measurement.2018.12.049

Liu, X. G., Zhu, W. C., Zhang, P. H., and Li, L. K. (2021a). Failure in rock with intersecting rough joints under uniaxial compression. *Int. J. Rock Mech. Min. Sci.* 146, 104832–832. doi:10.1016/j.ijrmms.2021.104832

Liu, Z. L., Ma, C. D., Wei, X. A., and Xie, W. B. (2021b). Experimental study on mechanical properties and failure modes of pre-existing cracks in sandstone during uniaxial tension/compression testing. *Eng. Fract. Mech.* 255, 107966–966. doi:10.1016/j.engfracmech.2021.107966

Liu, Z. L., Ma, C. D., Wei, X. A., and Xie, W. B. (2022a). Experimental study on the mechanical characteristics of single-fissure sandstone under triaxial extension. *Rock Mech. Rock Eng.* 55, 4441–4457. doi:10.1007/s00603-022-02876-x

Ma, J. J., Li, T. B., Zhang, Z., Roohollah, S. F., Mostafa, S., and Ma, C. C. (2025). Novel multifractal-based classification model for the quality grades of surrounding rock within tunnels. *Undergr. Space* 20, 140–156. doi:10.1016/j.undsp.2024.06.002

Niu, Y., Wang, J. G., Hu, Y. J., Wang, G., and Liu, B. L. (2023). Time-frequency domain characteristics of intact and cracked red sandstone based on acoustic emission waveforms. *Geomechanics Eng.* 34 (1), 1–15. doi:10.12989/gae.2023.34.1.001

Niu, Y., Zhou, X. P., and Berto, F. (2020). Evaluation of fracture mode classification in flawed red sandstone under uniaxial compression. *Theor. Appl. Fract. Mech.* 107, 102528. doi:10.1016/j.tafmec.2020.102528

Qin, Y., Xu, N. X., Han, J., and Zhou, W. J. (2022). Experimental study on the effects of geometric parameters of filled fractures on the mechanical properties and crack propagation mechanisms of rock masses. *Rock Mech. Rock Eng.* 56 (4), 2697–2716. doi:10.1007/s00603-022-03198-8

Sharafisafa, M., Shen, L. M., Zheng, Y. G., and Xiao, J. Z. (2019). The effect of flaw filling material on the compressive behaviour of 3D printed rock-like discs. *Int. J. Rock Mech. Min. Sci.* 117, 105–117. doi:10.1016/j.ijrmms.2019.03.031

Sun, B., Ren, F. Q., and Liu, D. Q. (2022). Research on the failure precursors of layered slate based on multifractal characteristics of acoustic emission. *Rock Soil Mech.* 43 (3), 1–12. doi:10.16285/j.rsm.2021.0879

Tian, H., Li, Z. H., Yin, S., Lei, Y. Y., Niu, Y., Wang, X. Y., et al. (2023). Research on infrared radiation response and energy dissipation characteristics of sandstone crushing under impact load. *Eng. Geol.* 322, 107171–171. doi:10.1016/j.enggeo.2023.107171

Wang, H., Fall, M., and Miao, S. (2024c). Characteristics of fracture changes and fatigue failure signals for siltstone under cyclic loading. *Int. J. Rock Mech. Min. Sci.* 174, 105645–645. doi:10.1016/j.ijrmms.2024.105645

Wang, X. R., Liu, S. X., Liu, X. F., Shan, T. C., Zhou, X., Xie, H., et al. (2024b). Mode I fracture propagation and post-peak behavior of sandstone: insight from AE and DIC observation. *Eng. Fract. Mech.* 302, 110093. doi:10.1016/j.engfracmech.2024.110093

Wang, X. R., Liu, X. F., Wang, E. Y., Liu, S. X., Shan, T. C., and Labuz, J. F. (2024a). Microcracking characterization in tensile failure of hard coal: an experimental and numerical approach. *Rock Mech. Rock Eng.* 57, 6441–6460. doi:10.1007/s00603-024-03827-4

Wang, Y. Q., Peng, K., Shang, X. Y., Li, L. P., Liu, Z. P., Wu, Y., et al. (2021). Experimental and numerical simulation study of crack coalescence modes and microcrack propagation law of fissured sandstone under uniaxial compression. *Theor. Appl. Fract. Mech.* 115, 103060–060. doi:10.1016/j.tafmec.2021.103060

Wray, R. A. L. (2009). Phreatic drainage conduits within quartz sandstone: evidence from the Jurassic Precipice sandstone, Carnarvon range, Queensland, Australia. *Geomorphology* 110, 203–211. doi:10.1016/j.geomorph.2009.04.007

Wu, D., Jing, L. W., Jing, W., and Peng, S. C. (2024). Cyclic loading and unloading strain equations and damage evolution of gypsum specimens considering damping effects. *Int. J. Damage Mech. 10567895241253735* 33, 808–833. doi:10.1177/10567895241253735

Wu, H., Kulatilake Pinnaduwa, H. S. W., Zhao, G. Y., Liang, W. Z., and Wang, E. J. (2019). A comprehensive study of fracture evolution of brittle rock containing an inverted U-shaped cavity under uniaxial compression. *Comput. Geotechnics* 116, 103219–219. doi:10.1016/j.compgeo.2019.103219

Xiao, W. J., Zhang, D. M., Li, S. J., and Lu, J. (2023). Fracture evolution and fracture mechanism of tunnel surrounding rock: a case study based on laboratory tests and theoretical analysis. *Fatigue and Fract. Eng. Mater. and Struct.* 46 (7), 2617–2638. doi:10.1111/ffe.14021

Yang, L. Y., Zhang, F., You, J. X., Man, D. H., Gao, J., and Liu, W. (2024). Mechanical behaviour and spatial fracture characteristics of weakly filled granite with different diameters under uniaxial loading revealed by 3D DIC and AE monitoring. *Bull. Eng. Geol. Environ.* 83 (6), 217. doi:10.1007/s10064-024-03683-0

Yang, S. Q., Huang, Y. H., Tian, W. L., and Zhu, J. B. (2017). An experimental investigation on strength, deformation and crack evolution behavior of sandstone containing two oval flaws under uniaxial compression. *Eng. Geol.* 218, 35–48. doi:10.1016/j.enggeo.2016.12.004

Zhang, J. Z., and Zhou, X. P. (2023). Integrated acoustic-optic-mechanics (AOM) multi-physics field characterization methods for a crack: tension vs. shear. *Eng. Fract. Mech.* 287, 109339. doi:10.1016/j.engfracmech.2023.109339

Zhang, X. A., Wen, G. C., Zhu, Z. M., Luo, Q. M., and Liu, J. (2024). Dynamic propagation characteristics of mode I crack in infilled jointed rock masses under impact load. *Rock Soil Mech.* 45 (2), 396–406. doi:10.16285/j.rsm.2023.5237

Zhang, X. P., Zhang, Q., and Wu, S. C. (2017). Acoustic emission characteristics of the rock-like material containing a single flaw under different compressive loading rates. *Comput. Geotechnics* 83, 83–97. doi:10.1016/j.compgeo.2016.11.003

Zhao, Z. H., Suo, Y. F., Liu, Z. N., Zhao, X. G., Liu, B., Zhao, Y. Y., et al. (2024). Effect of pre-existing infilled fracture on characteristics of failure zones around circular opening. *Comput. Geotechnics* 169, 106228. doi:10.1016/j.compgeo.2024.106228

Zheng, Q. Q., Qian, J. W., Zhang, H. J., Chen, Y. K., and Zhang, S. H. (2024). Velocity tomography of cross-sectional damage evolution along rock longitudinal direction under uniaxial loading. *Tunn. Undergr. Space Technol.* 143, 105503. doi:10.1016/j.tust.2023.105503

Zhou, X. P., Niu, Y., Cheng, H., and Berto, F. (2021). Cracking behaviors and chaotic characteristics of sandstone with unfilled and filled dentate flaw. *Theor. Appl. Fract. Mech.* 112, 102876–876. doi:10.1016/j.tafmec.2020.102876

Zhu, Q. Q., Li, C. J., Li, X. B., Li, D. Y., Wang, W., and Chen, J. Z. (2022). Fracture mechanism and energy evolution of sandstone with a circular inclusion. *Int. J. Rock Mech. Min. Sci.* 155, 105139–139. doi:10.1016/j.ijrmms.2022.105139

Zou, Q. L., Ning, Y. H., Zhang, B. C., Tian, S. X., Jiang, Z. B., and An, Y. Q. (2023). Mechanical properties and failure characteristics of sandstone under ramp loading paths. *Geomechanics Geophys. Geo-Energy Geo-Resources* 9 (1), 39. doi:10.1007/s40948-023-00574-8